

## LIMNOLOGY and OCEANOGRAPHY: METHODS



Limnol. Oceanogr.: Methods 2025

© 2025 The Author(s). Limnology and Oceanography: Methods published by
Wiley Periodicals LLC on behalf of Association for the Sciences of
Limnology and Oceanography.
doi: 10.1002/lom3.10724

### **NEW METHODS**

# GelCam: Visualizing sinking particle flux via a polyacrylamide gel-based sediment trap

Yixuan Song <sup>1</sup>, <sup>1</sup>\* Melissa Omand, <sup>1</sup> Colleen A. Durkin <sup>1</sup>, <sup>2</sup> Margaret L. Estapa <sup>1</sup>, <sup>3</sup> Ken O. Buesseler <sup>4</sup>

Graduate School of Oceanography, University of Rhode Island, Narragansett, Rhode Island, USA; <sup>2</sup>Monterey Bay Aquarium Research Institute, Moss Landing, California, USA; <sup>3</sup>School of Marine Sciences, Darling Marine Center, University of Maine, Walpole, Maine, USA; <sup>4</sup>Woods Hole Oceanographic Institution, Woods Hole, Massachusetts, USA

#### **Abstract**

Sinking particles play a key role in the biological carbon pump. While previous studies have analyzed particulate carbon flux over timescales of days to years, few have been able to resolve flux variability on shorter, hourly scales at multiple depths simultaneously. This study uses an array of upward-facing cameras, built from off-the-shelf components for under \$500 each, to visualize particle fluxes at multiple depths during the EXPORTS campaign in 2018 in the North Pacific. This manuscript is the first comprehensive description of this tool, called GelCam, which captures a time-lapse image sequence at 20-min intervals of particles that settle into a polyacrylamide gel layer located at the base of a sediment trap tube. Methods are described for the design and post-processing pipeline, in addition to two proxy methods for estimating the total particulate organic carbon flux. The GelCam-derived fluxes modeled from individual particle images show strong agreement with the ground-truth data obtained from coincident trap measurements. This approach helps address the need for accessible, open-source tools to more broadly observe and quantify the role of episodic particle flux events across the global oceans.

The ocean sink provides a net uptake of approximately  $2.8 \times 10^{15}\,\mathrm{g}$  of carbon from the atmosphere each year, which accounts for more than 25% of anthropogenic  $\mathrm{CO}_2$  emissions (Friedlingstein et al. 2023). The global magnitude of phytoplankton-derived or biological carbon export is estimated to be  $\sim 10^{15}\,\mathrm{g/yr}$  of carbon transferred from the surface ocean to the interior (Henson et al. 2011; Nowicki et al. 2022; DeVries and Weber 2017). One of the primary mechanisms driving this biological carbon pump is the passive sinking of particulate organic carbon (POC), known as the "gravitational pump," which plays a crucial role in regulating carbon sequestration and predicting climate change effects (Nowicki et al. 2022; Bisson et al. 2020). There are many sources of uncertainty that

\*Correspondence: yixuan.song@uri.edu

This is an open access article under the terms of the Creative Commons Attribution-NonCommercial License, which permits use, distribution and reproduction in any medium, provided the original work is properly cited and is not used for commercial purposes.

Associate editor: Mike DeGrandpre

complicate modeling of the biological carbon pump. Aggregation (Burd and Jackson 2009; Alldredge and Gotschalk 1988) disaggregation (Briggs et al. 2020; Song et al. 2023), and microbial degradation occurring on particles (Collins et al. 2015) alter particle size and contribute to the high variability in the sinking velocity of marine particles (McDonnell and Buesseler 2010). Additionally, consumption and production by zooplankton and fish (Cavan et al. 2017), vertical mixing (Dall'Olmo et al. 2016), and eddy subduction (Omand et al. 2015) interact with passively sinking particles. Moreover, spatial and temporal variability further complicates the modeling of global biogeochemical cycles (Piao et al. 2013; Sierral et al. 2007). These challenges, along with observational limitations in remote areas and deep sea environments, add uncertainty to our understanding of carbon flux within the ocean (Henson et al. 2022; Wilson et al. 2022).

Sediment traps provide a direct measurement of sinking marine particles, as the downward carbon flux can be retrieved from the total organic matter captured over a period of time within a fixed collection area of a tube or a funnel (Buesseler et al. 2007). Traditional sediment trap measurements provide an integrated carbon flux sample collected over time scales ranging

from days to months (Buesseler et al. 2007). Various post-analysis steps are necessary for most traditional sediment trap measurements. For example, Müller and Suess (1979) applied elemental combustion analysis to measure the organic carbon content in sediment trap samples. Durkin et al. (2021) used microscopic imaging techniques to analyze particles preserved in the polyacrylamide gel. These analyses are labor-demanding and are limited in their ability to assess episodic variations on timescales of hours.

In situ time-lapse imaging, with the potential for onboard data processing, can alleviate some of these demands. Imaging techniques have been used to detect episodic particle fluxes to the seafloor (Billett et al. 1983) and to estimate the sinking speeds of marine snow aggregates within sediment traps (Asper 1987). More recently, upward facing cameras have been used during short-term deployments. Bishop et al. (2016) and Bourne et al. (2021) developed the Optical Sedimentation Recorder (OSR) to quantify carbon fluxes via optical attenuance measurements, deployed on surfacetethered buoys and autonomous Carbon Flux Explorer (CFE). Bishop et al. (2016) estimated POC flux using empirical relationships between particle size and carbon content, while Bourne et al. (2021) further calibrated volume attenuance flux against POC and analyzed particle size distributions with particle classes. Additionally, McGill et al. (2016) developed a novel instrument, the Sedimentation Event Sensor (SES), to image particle samples collected by a funnel-shaped sediment trap. Huffard et al. (2020) deployed the SES and analyzed particle images collected over a 2-h period to evaluate how short-term factors influence particle flux to the deep sea. These advancements have greatly improved our ability to observe and quantify particulate flux. However, the high cost of existing imaging systems limits their extensive use, creating a need for an affordable instrument with onboard rapid analysis capabilities.

To better understand and constrain temporal variability in particle fluxes and identify the ecological sources that drive these variations, we have developed a novel, affordable, and easy-to-deploy instrument, named "GelCam." This instrument allows for a rapid evaluation without extensive post analysis and chronological diagnosis of particle identities. Here we demonstrate the GelCam design and analyze episodic particulate organic carbon fluxes from nine datasets collected during the NASA EXPORTS (EXport Processes in the Ocean from Remote Sensing) field campaign in the North Pacific in 2018. The image post-processing contains a particle tracking algorithm and particle classification, which provide the arrival time and morphology of each particle. The GelCam, with the framework of imaging processing, can be applied to quantify the particle flux using two methods, one based on cumulative particle areas and the other based on the particle tracking and classification results. Here we model the particulate organic carbon from particle images and assess the performance by comparing the fluxes between GelCam and coincident geochemical and microscope-based methods. We discuss the benefits of using the GelCam to extract quantitative carbon flux and facilitate modeling of the biological carbon pump.

#### Materials and procedures

#### GelCam design

The GelCam is a time-lapse camera system designed to pair with a particle-intercepting sediment trap. This manuscript describes the first prototype of the system (subsequent improvements are mentioned where appropriate) which was paired with a cylindrical trap with an outer diameter of 127 mm and a total length of 700 mm (Fig. 1A). The trap tube had a swimmer exclusion baffle with cell openings of about 1 cm, allowing small particles to pass through. A lid closure method used a bungee that was mounted to a horizontal bar spanning a lower section of the tube. The open tube bottom was attached to the camera system with opposed flanges and an o-ring face seal. Before sealing the camera to the tube, a shallow container with a transparent bottom was filled with a  $\sim 10$  mm thick layer of polyacrylamide gel and placed at the base of the trap and served to retain deposited particles.

The GelCam housing was composed of an optically clear 1 in. thick acrylic top lid, a cylindrical acetal resin (Delrin) tube, and an acetal resin bottom lid (Fig. 1A) with a nominal pressure rating of 300 m. The top lid contained a light emitting diode (LED) ring with an outer diameter of 120 mm and width of 4 mm that was potted in a clear epoxy resin. Keeping the light as close as possible to the base of the gel cup eliminated direct light and reflections, allowing only diffuse, scattered light to enter the camera. Brackets fabricated by 3D printing techniques and designed to secure the batteries and electronics were integrated within the housing. We used 7 packs of 12 V (nominal) stacks, each consisting of 4 CR123A batteries, yielding 134 Watt-hrs. The batteries were used to power an Arduino Nano microcontroller, a Raspberry Pi Zero WiFi singleboard computer, a Raspberry Pi camera module, and the LED ring. The low-power Arduino was used to duty cycle the R-Pi Zero, enabling a maximum deployment duration of 8 days with photos every 20 min. The camera was mounted facing upwards toward the gel container with a viewing axis aligned with the central axis of the sediment trap, enabling us to image nearly the entire area of the base of the gel-filled cup.

The camera module had a sensor resolution of  $2592 \times 1944$  pixels. The lens used in the 2018 expedition provided a field of view (FOV) of approximately 55.2 mm  $\times$  41.4 mm, which translated to a pixel resolution of 21.3  $\mu$ m per pixel on the upper surface of the end cap. We calibrated the cameras before each deployment, with a focal plane set to the deepest layer of the gel where particles accumulated and a focal range of approximately 2 cm. The Arduino Nano was programmed to duty cycle the R-Pi at a 20-min interval. However, due to drift in the oscillator onboard the ATMEGA328P microcontroller, the actual time interval varied up to a few minutes between

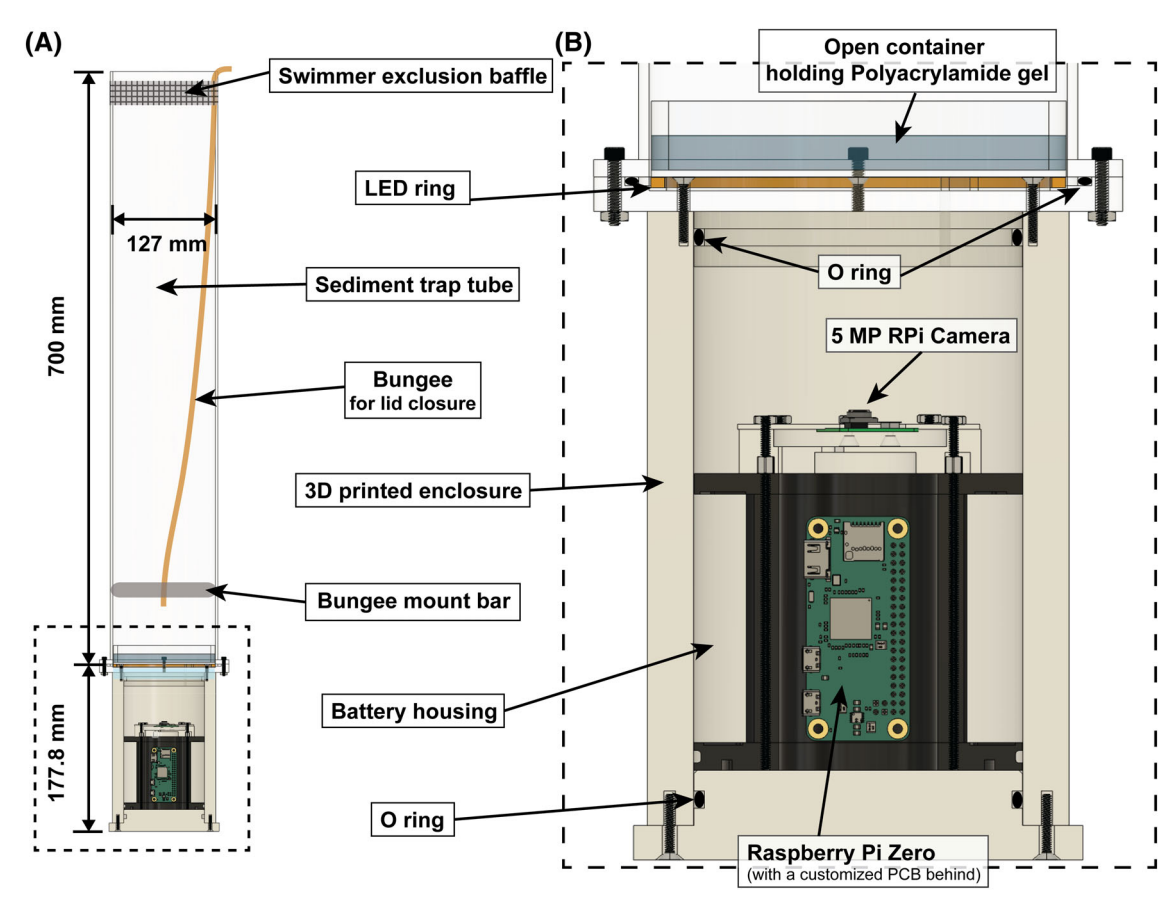


Fig. 1. Schematic diagram of the GelCam system: (A) overview of the sediment trap with the GelCam attached to the bottom, and (B) detailed cross-section view within the enclosure.

deployments. To address this issue, we also integrated an accurate real-time clock (DS3231), which logged the time stamp for each image. Later versions of this system have replaced the Arduino-based ATMEGA328P with a PIC16F1847 microcontroller unit (Microchip Technology) which improves the timing accuracy and power consumption substantially. Images in .jpeg format were captured with an automatic camera setting and archived on a 64 GB SD card within the R-Pi Zero. The total cost of the off-the-shelf components was less than \$500, and a bill of materials is provided in Table S3 of the Supporting Information.

#### Cruises and sampling platform

Three GelCams attached to three depths on each surface-tethered trap (STT) array were deployed from the R/V *Roger Revelle* near Ocean Station Papa (50°N, 145°W) during the EXPORTS North Pacific cruise. The cruise conducted three repeating sampling cycles identified as Deployment 1, 2, and 3, from 15 August to 05 September 2018 (Table 1) (other NASA EXPORTS publications referred to deployment duration as "epoch") resulting in nine total GelCam datasets. The overall deployment scheme is presented in Siegel et al. (2021) and sediment trap details are presented in Estapa et al. (2021).

GelCams were attached at depths corresponding to 95, 145, and 195 m in Deployment 1. Storm-induced damage broke the wave-damping bungee, which resulted in an increase to 105, 155, and 205 m, respectively, during Deployments 2 and 3. Details for the preparation of the sediment trap tubes and polyacrylamide gels are described in Durkin et al. (2021).

GelCams deployed during Deployments 1 and 3 collected more than 400 images each during more than 6 days of deployments. GelCams during Deployment 2 recorded about 360 images over 5 days. The camera system infrequently encountered a compression issue while transmitting the data to the SD card, leading to anomalous images being saved. These corrupted image files could not be used for any image processing. A manual check identified 24 images with quality issues out of 3677.

#### Imaging processing procedures

#### Color decomposition to remove ambient light variations

An image processing pipeline was developed for the GelCam images. Each raw .jpeg image (*see* example in Fig. 2A) shows the LED near the outer edge of the gel cup (large white circle), the bar holding the bungee, and darkened areas of the

**Table 1.** Summary of sampling locations.

Deployment		Location	Dates	Depths	# of images
Deployment 1	STT 1	Subarctic North Pacific	15–21 Aug 2018	95 m	445
	STT 2	50.1°N, 145.1°W		145 m	410
	STT 3			195 m	443
Deployment 2	STT 1	Subarctic North Pacific	24–28 Aug 2018	105 m	369
	STT 2	50.4°N, 145.1°W		155 m	368
	STT 3			205 m	341
Deployment 3	STT 1	Subarctic North Pacific	31 Aug to 05 Sep 2018	105 m	442
	STT 2	50.6°N, 144.9°W		155 m	446
	STT 3			205 m	413

background where the clear tube was mounted to the STT frame and near the top at the lid attachment.

Because the GelCam was adapted for an existing sediment trap design, there were multiple image processing challenges that could potentially be avoided in future iterations, such as the clear tube that allows ambient light through, the bungee bar, and visible trap superstructure. We discuss some of these improvements in the Discussion section. However, to best utilize the images we had, we created a static mask to exclude the cup edge, the bungee mount bar, and other bright background objects from the FOV. During daytime, ambient sunlight caused portions of the background to appear in a green-blue hue, even at the deepest sampled depth of 205 m. After decomposing the images into the green, blue, and red channels (Fig. 2B,D), we found that the red channel was effective at filtering out the ambient light since ambient red wavelengths are strongly attenuated by seawater in the upper few meters. The red channel image was subsequently converted to gray scale for region of interest (ROI) identification. It should be noted that the conversion from raw sensor data to RGB images involves demosacking (Gunturk et al. 2005), during which red channel pixel intensities may include interpolated contributions from the neighboring blue and green pixels. The demosacking still introduced low-level background noise into the red channel in our data.

The temporal variations in the blue and green channel were effective at illustrating the day-and-night cycle in ambient sunlight. Since we are potentially interested in animal-driven diurnal variations of particle flux, it was crucial that we account for any variations in particle detection likelihood or contouring that might arise due to the variations of background light. Since the particles occupied less than 7.5% of the field of view, the blue and green pixel intensity (spatially averaged across each image) provided a fairly reliable representation of the overall ambient light changes over time (Fig. 2C). The variations were low during nighttime, while noticeable peaks were observable around mid-day. A strong correlation was found between the lighting variations within the green and blue channels and concurrent measurements of surface light levels obtained from a Photosynthetically Active

Radiation (PAR) sensor deployed on a WireWalker (Supporting Information, Fig. S3). The example track sequence of a single long fecal pellet over time shown in Fig. 3 highlights the RGB color variations between night and day, with the background color turning green during the daylight hours. The day–night pattern was not evident in the normalized red channel, and so by using only the red channel for particle edge detection, we markedly reduced the sensitivity to background light variations. Selection of the red channel also had the effect of eliminating the color variation associated with the trap tube components that were far away from the illumination source, such as the tube bracket and top lip (*see* the darker concentric rings in Fig. 2A compared to D).

#### Background removal

The next step in image preparation was the masking of the static parts of the image that contained strongly contrasting tube parts close to the illumination source, such as the bungee bar and knot (Fig. 2D). Here we used a proper orthogonal decomposition (POD) method, which has been proven effective in particle image velocimetry (PIV) (Mendez et al. 2017) and particle tracking (Song and Rau 2022). In our current configuration, we observed particle movements and rotations driven by local circulations and small-scale flows acting on the sediment trap. Such movements made the application of POD-based background removal possible. We implemented this by applying a static mask first to all images in the red channel, followed by a singular value decomposition. Subsequently, we eliminated the first principal component and reconstructed the image frames. Figure 2E shows the resulting background-removed product of the masked red-channel image in D. Using this method, particles were successfully preserved while the background was eliminated.

#### Particle contouring

Next we developed a double-threshold method to convert particles in the grayscale image to binary form. First, we computed the Otsu threshold (Otsu 1979) for each image frame after the background removal. We then averaged these thresholds to establish a global black-and-white cutoff. The first round of binarization was mostly effective, but we found that

**Fig. 2.** Pipeline of image pre-processing procedures, with (**A**) original captured image, (**B**) decomposed images in green and blue channels, (**C**) example day-and-night cycle represented by the average pixel intensities in green (solid line) and blue (dotted line) channels, (**D**) red channel image, (**E**) masked grayscale image after background removal, and (**F**) binarized image with particles outlined. *See* Fig. S3 in Supporting Information for correlations between green/blue channels and PAR signals.



**Fig. 3.** Example tracking series from Deployment 3 STT 1. Six tracked trajectories are shown over a static mask, with start and end timestamps displayed. The right panel illustrates the morphological changes of a tracked long fecal pellet over time. The first image in this deployment was captured at 16:54:02 on 31 Aug 2018, and the last image at 06:26:46 on 06 Sep 2018. In the right panel, three black dots indicate skips of more than three tracking images, while a single dot denotes a skip of exactly three intervals (approximately 80 min).

using a global threshold did not completely outline particles with looser structures, such as aggregates, which had segmented shapes. To remedy this, we set an additional but lower threshold by subtracting from the global threshold three standard deviations of the grayscale intensities of all pixels in the first image (e.g., Deployment 3 STT 1 had upper and lower thresholds of 56.7 and 36.7 out of 255). The lower cutoff value retained relatively dimmer pixels, often bridging between aggregate segments, although it also included some background noise. Here we retained pixels that passed the lower threshold if they connected with pixels that had passed the first global threshold. Lastly, we applied an area filter with a 50-pixel minimum (ESD (equivalent spherical diameter)  $\sim 170 \ \mu m$ ) to exclude noise features and small particles that lacked sufficient morphological details for classification. We compiled a table assigning each particle a unique index and summarizing the images and morphology of particles in all image frames. Figure 2F shows an example of the particles that passed our binarization method, outlined in red.

#### Particle tracking

We next implemented a particle tracking method to extract the particle motion within the gel. The surface tethered sediment trap experienced fairly strong vertical and rotational wave-driven motions during deployment. For the first two deployments in the North Pacific, the gel cup was also able to freely rotate within the tube, and this enhanced the rotational movements of the particles within the gel. We recommend that readers reproducing these methods take steps to secure the cup to the tube or GelCam lid to reduce this motion. In our study, the particles experienced marked horizontal swirling motions relative to the camera throughout the deployments (see Supporting Information videos). The high viscosity of the gel helped to keep these motions fairly smooth, with strong auto-correlation between the particle motions that were straightforward to track by eye and with our bulk motion routines. To enable particle tracking between subsequent images, we first utilized particle image velocimetry (PIV) to capture the bulk movement. We used the open-source PIVlab code (Thielicke and Stamhuis 2014) to implement a single PIV pass to detect the velocities associated with the bulk motion. A square evaluation window with a size of 320  $\times$  320  $(x \times y)$  pixels was selected based on the smallest particle density (at least eight particles within one interrogation window) and the maximum distance particles seemed to travel within the 20 min image interval (e.g., the 99% percentile in Deployment 1 STT 1 was 54.5 pixels). This window size also ensured sufficient bright pixels for cross correlation in the first few frames. We set the window overlap at 50% in both x and y directions. Following this, a two-dimensional Gaussian regression model (Nobach and Honkanen 2005) provided a sub-pixel estimation. Additionally, we applied a universal outlier detection after the single pass to eliminate inaccurate vectors (Westerweel and Scarano 2005). The PIV analysis yielded a bulk velocity field of 15  $\times$  11 vectors. To approximate

particle movement between frames, we applied a twodimensional interpolation method to each particle's centroid position.

Next, we performed another cross-correlation method to precisely track each particle's movement between adjacent frames. Here we created two interrogation windows,  $w_1$  and  $w_2$ , from two successive frames. We defined the first interrogation window,  $w_1$ , as a rectangular box around a particle indexed i after the contouring. Each side of the window had a minimum distance of 8 pixels from the particle's edge. The second interrogation window,  $w_2$  in the following frame, was centered on the guessed position, based on the particle's estimated centroid after interpolating the PIV vectors. We expanded this window size by 16 pixels for large particles (if the longest particle dimension was greater than 16 pixels), and by 8 pixels if the particle was small (less than 16 pixels). We then conducted a cross-correlation search within  $w_2$  to find the best match. The location that generated the best correlation, with a correlation coefficient > 0.7 and a distinct peak in the correlation plane, was allocated as position i' in the next frame. If this location matched a particle *j* in the second frame (i = i'), we linked the two particle indices i and j in our tracking series. Conversely, we considered particles without matches as new arrivals. Figure 3 presents six representative tracking trajectories recorded during Deployment 3 STT 1. The start and end timestamps confirm the application of particle tracking over a period exceeding 6 days. On the right side of Fig. 3, a tracking example of a long fecal pellet is presented in its raw RGB color format. Initially observed near the bungee mount bar on 01 September 2018, the fecal pellet subsequently underwent translation, deformation, re-orientation, and variations in background lighting (second and third rows). In the fourth row, smaller particles are seen moving past the fecal pellet within the gel layer, while the algorithm continues to track this long fecal pellet. This fecal pellet remained within the FOV until the final image was captured by the GelCam on 06 September 2018. To further confirm the accuracy of the tracking results, a random subset of 500 particle sequences was manually examined from a total of 43,286 sequences. No mismatches were identified in the tracking data.

In some cases, two particles overlapped and crossed each other (28% of the total). The overlap issue became increasingly problematic in the later deployment stage as more particles appeared in the FOV. In these cases, we flagged instances where two or more particles, such as  $i_1$  and  $i_2$ , corresponded with the same match j in the next frame. Moreover, we also ran our tracking algorithm in reverse chronological order to detect "separation" events, the reverse of overlapping. In addition to 500 randomly chosen particle sequences, we manually examined 186 overlapping cases. After applying the algorithm above, the tracking methods successfully detected and differentiated the overlapping particles in all but two cases. This result convinced us that our approach to distinguish overlapping particles was successful.

The final challenge we needed to resolve was cases where the particles moved past a masked feature such as the bungee bar. The bar, shown in Fig. 2A, resulted in particles leaving and re-entering the FOV over durations that were longer than the consecutive frame interval. Here, we extended the duration of predicted centroids over 12 h using the PIV vectors. Unpaired particles were defined as those appearing in the last of the tracking series without any matches since then. We compared the distance between the centroid of a newly arrived particle and predicted locations of unpaired particles on their estimated trajectories, based on the new arrival time. If the distance was less than 32 pixels, this newly arrived particle would undergo the same cross correlation method with other unpaired particles. Based on the same criteria described above, two particles were considered a match if the correlation coefficient was high with a unique peak in the correlation plane.

Not all particles were traceable from their arrival through the entire deployment to the last image, and some, such as swimmers (organisms that actively entered the trap and were not part of the passive flux) were discounted from the particle flux counts. Some particles drifted off frame, while others abruptly disappeared or had an intensity that faded below the threshold. To deal with this, we used a labeling system that indicated whether the particle disappeared at an edge, faded in FOV, or was manually identified as a swimmer. Of the 43,286 tracked particles, 10,169 were tracked from arrival to the final frame, 7439 moved out of the FOV, and 132 were categorized as large swimmers. The rest of the tracking sequences were labeled as particles faded in FOV, weak cross-correlations, and small areas. Additionally, some particles were found to enter the FOV from the sides, suggesting that they could be re-entering the image after arriving and leaving at an earlier time. Fourteen percent of the total particles were flagged as a potential re-entry. Detailed diagnoses with labels can be found in Table S1 in the Supporting Information.

#### Particle classification

Following Durkin et al. (2021), we classified each unique particle into one of six categories, as summarized in Fig. 4. These particle categories were developed based on detailed microscope images of the same gels as those presented here. However, due to the image quality and color variations inherent in the GelCam prototype, the machine learning tools (Amaral and Durkin 2025) that were developed for the microscope images were not optimal for these ROIs. Additionally, overly saturated colors caused many particles to appear completely white, making it impossible to extract color information. Because of the relatively small number of GelCam images and the quantity of classified images needed to train a supervised model, we decided to manually assign each particle an identity based on their unprocessed colored sub-images. Aggregates had irregular shapes and loose structures. Large

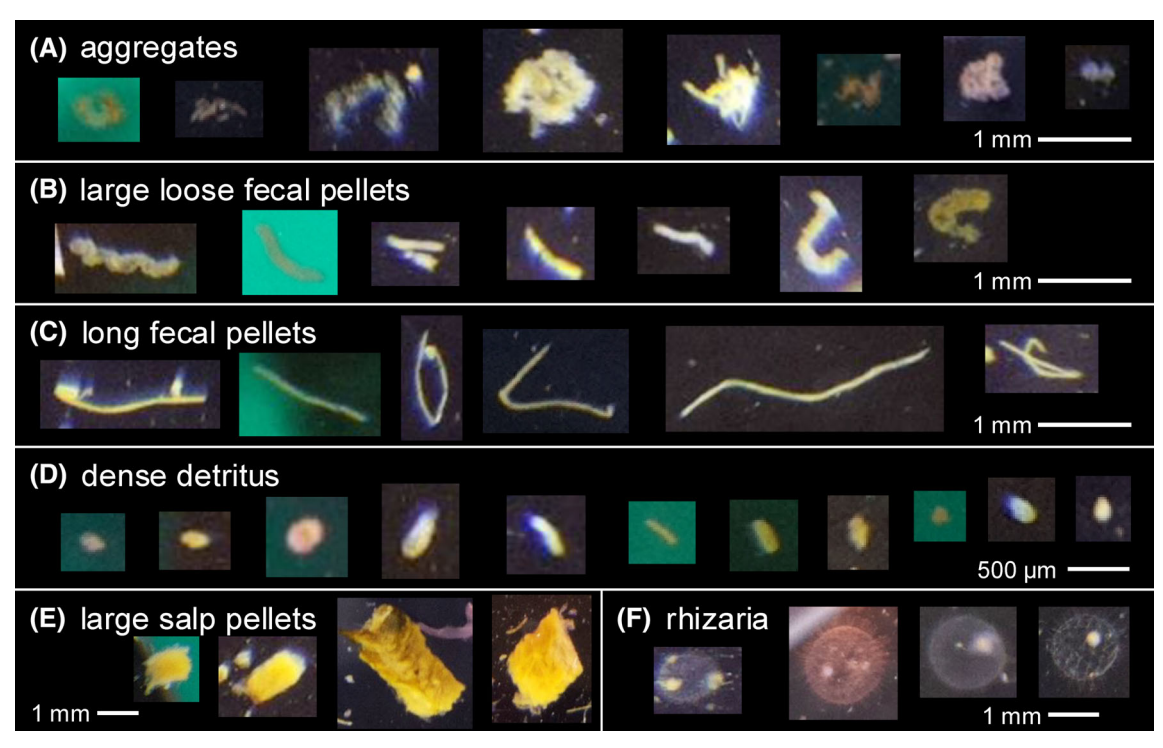


**Fig. 4.** Passively sinking particle classes with example sub-images, including (**A**) aggregates, (**B**) large loose fecal pellets, (**C**) long fecal pellets, (**D**) dense detritus, (**E**) large salp pellets, and (**F**) rhizaria.

loose fecal pellets were produced by large zooplankton (e.g., pteropods) and were often elongated with dense coloring. Their shapes were more regular than aggregates and composed of one or a few distinct sub-units. Long fecal pellets were thin and elongated with smooth edges. Due to the lower pixel resolution, we classified most small ellipsoid particles as dense detritus, which likely include both small fecal pellets and fecal detritus. Following the study that has been published on the presence of salps (Bruland and Silver 1981), we categorized their pellets as large and golden-colored, with nearly rectangular shapes. We also detected a few rhizarians, primarily Phaeodaria. Large zooplankton were excluded through the particle tracking and labeling system, while smaller zooplankton were occasionally observed and subsequently removed during manual classification. We differed from the classification suggested by Durkin et al. (2021) in that we did not identify any phytoplankton cells or mini pellets, since these usually had a size of less than 50  $\mu$ m in ESD (Gowing and Silver 1985) and were smaller than the size we felt confident in identifying.

#### **Assessment**

#### Modeling carbon fluxes

Tracking "new" particle arrivals using the timelapse method enables new insights into carbon flux variability, but it also raises new challenges. Because this is a new method, with imaging tools that are still undergoing optimization, we tried

two different methods for establishing an image-based carbon flux proxy. The first—hereafter referred to as the "white pixel method"—summed up the area of all white pixels in the binarized image. The white pixel method aims to quickly obtain the bulk particle accumulated areas using a single black-and-white threshold. This method is sensitive to the day-night variations in ambient light. Figure 5 shows the time-varying percentage FOV coverage, calculated through cumulative particle area divided by the entire FOV. Brighter ambient light conditions tended to cause an apparent reduction in size or result in some particles dropping below the detection limit, which resulted in a reduction of white pixel area during the daytime (see gray line, Fig. 5A). A linear correction was developed that utilized the difference in light intensity relative to the nighttime blue channel levels. The percentage of pixels affected by the brighter background, primarily due to the interpolation artifacts from blue and green channels, was then computed based on the interpolated estimate and the captured particle areas. We define "excess blue light" intensity as the difference in blue light intensity between the daytime and the average nighttime values (e.g., see the range indicated in Fig. 2C). We correlated the excess blue light with the percentage of quenched pixels, allowing for a corrected white pixel estimate for each daytime time stamp (see red line, Fig. 5A). Detailed steps for this method can be found in the Supporting Information.

The second method, hereafter referred to as the "trackingbased method," used a conservative version of particle

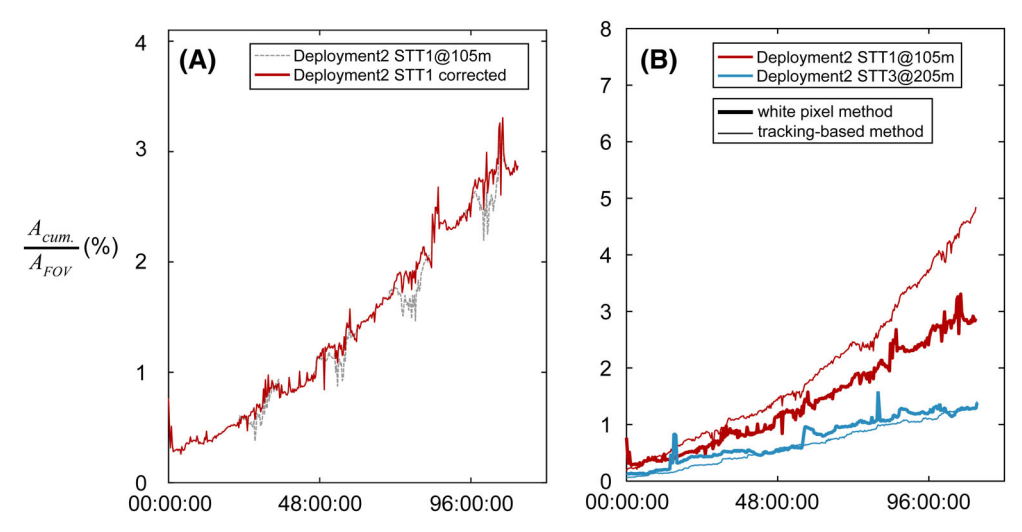


**Fig. 5.** Cumulative particle areas as a function of time for selected samples in the North Pacific dataset. Panel (**A**) consists of the number of white pixels from binarized images (dotted gray line) and the lighting-corrected cumulative areas (red solid line) during Deployment 2 STT 1 at 105 m. Panel (**B**) shows cumulative particle areas using the white pixel method (thick lines) and using the tracking-based method (thin lines) for Deployment 2 STT 1 at 105 m and STT 3 at 205 m. Thin lines only focus on passively sinking particles classified following Fig. 4. See Fig. S5 for comparisons of all measurements.

tracking and classification. We did not sum up all tracking series at their apparent time of arrival. Otherwise, particles could be counted more than once due to interruptions in the tracking sequences, which was also a common issue applying the particle tracking. Rather, we implemented a frame-based calculation. Given a specific image frame with a timestamp, we first found all identified particles that had been contoured. Next, we used tracking sequences to trace each particle to its state upon arrival. Using the size and shape upon arrival is intended to exclude any potential degradation or other morphological changes over time. Next, following the labeling system described above, we added all particles that left the FOV before this timestamp and subtracted particles that came into the FOV from the edges. This operation efficiently corrected the cumulative particle areas influenced by gel movement. It is likely that this method could underestimate the particle size for those arriving during the day. However, the particle size of individual tracked particles did not show a distinct diurnal pattern. Although it requires more processing time, an advantage of the tracking-based method over the white pixel method is that it allows an estimate of the time of arrival of particular particle types/sizes.

The particulate organic carbon of each new particle was determined following the equation  $C = A \cdot V^B$  listed in Durkin et al. (2021), where C is the carbon per particle (mg), A is the scaling coefficient, V is the particle volume ( $\mu$ m<sup>3</sup>), and B is a unitless exponent. The exponent B characterizes the porosity of a given type of particle as its size increases. Table S2 in Supporting Information lists shapes, volumes, and modeling parameters of each particle type. We followed Durkin et al. (2021) closely to model the POC flux. It should be noted that dense detritus was poorly resolved in our images relative to the microscope images in that paper. This

particle type could be a mixed group of aggregates and fecal pellets.

Swimmers were excluded from the analysis when calculating passively sinking particle fluxes. We extracted particle areas from the tracking series and summed six classified particle categories. Figure 5B compares the two methods of quantifying cumulative particle areas in Deployment 2, where the symbolized curves represent the classification-based integrated areas and the others are the white-pixel-based cumulative particle areas. The two methods showed great agreement with each other, but the approach based on tracking and classification generated smoother responses. Random spikes were eliminated because the tracking series excluded air bubbles and swimmers. These symbolized curves did not show any valleys because we only extracted particle areas at the time of arrival. In other words, using the particle tracking automatically eliminates ambient light-induced area variations. Moreover, this approach accounted for particles leaving and entering the unmasked area, which also explained the small deviation from using white pixels only. See Fig. S5 for measurements of all stations using both methods.

# Particulate organic carbon flux compositions and efficiency of carbon flux

The tracking based method was used to model the net POC flux for each GelCam deployment categorized according to particle type (stacked bars, Fig. 6). These results are compared to the total carbon fluxes measured directly in the bulk flux tubes (open circles) (Estapa et al. 2021) and modeled POC fluxes using microscope images and classification (crosses) (Durkin et al. 2021). In general, the GelCam-modeled POC flux had fairly good agreement with the other methods in the shallower traps (STT 1 at 95 m and STT 2 at 155 m), and

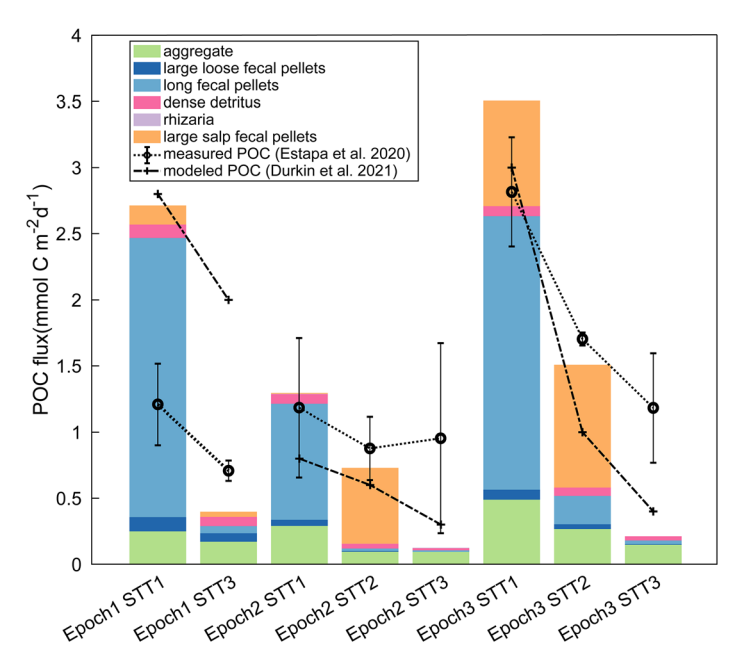


**Fig. 6.** Modeled particulate organic carbon (POC) flux by each type during EXPORTS NP. Particulate organic carbon fluxes are also compared with measured data in formalin-poisoned trap tubes (Estapa et al. 2021) and modeled ones based on microscopic images (Durkin et al. 2021).

tended to underestimate the flux relative to the other measurements at STT 3 (at 205 m). We suspect that a primary reason for this discrepancy at depth is that the GelCam could not resolve small particles. Particles with an equivalent diameter smaller than 100  $\mu m$  could contribute up to 46% to the total POC at STT 3 during the North Pacific EXPORTS cruise (Durkin et al. 2021), whereas the detection limit of the GelCam was 170  $\mu m$ . Additionally, visual sensors have a difficult time detecting nearly transparent or disaggregating materials as particles became further degraded with depth.

The particle-classified GelCam derived fluxes were primarily composed of aggregates, large loose fecal pellets, long fecal pellets, and dense detritus during EXPORTS-NP. Long fecal pellets were dominant at STT 1, contributing 67% to the total POC fluxes. Aggregates, large loose fecal pellets, and dense detritus were less abundant but still contributed a significant part compared to rhizaria. At STT 3, aggregates were the most abundant and contributed up to 70% of the total carbon. Salp pellets were observed as one of the dominant particle types in the microscope analysis of the gels (Durkin et al. 2021; Steinberg et al. 2023). Similarly, we found that large salp pellets dominated the GelCam-based POC calculations for some deployments. For example, two huge salp pellets constituted 79% of the total carbon during Deployment 2 STT 2.

Transfer efficiency was highly variable across particle types. Here we defined  $T_{100}$  as transfer efficiency, which is the ratio of carbon flux at 100 m below the reference depth (defined as the depth of STT 1) and carbon flux at the reference depth

(i.e.,  $POC_{STT3}/POC_{STT1}$ ). The transfer efficiency in the NP was 14%, 9.6%, and 6.0%, respectively. The percentage was lower than the sediment trap measurements (Estapa et al. 2021) due to the low modeled POC fluxes at STT 3. Missing small particles could be one main reason.

The GelCam emphasized the important role of fecal pellets in carbon flux during the EXPORTS North Pacific campaign. In agreement with previously published results (Durkin et al. 2021), long fecal pellets were the dominant particle type in the traps near the surface. Long fecal pellets and large loose fecal pellets had very high attenuation (> 97.0%). For example, during Deployment 2 STT 3, we did not see any large loose fecal pellets; only 1.3% carbon of long fecal pellets remained compared to STT 1. We did not calculate the transfer efficiency of large salp fecal pellets due to the low sample number.

Aggregates and dense detritus had the highest transfer efficiencies, which varied from 30% to 68%. One likely reason would be the conversion from other particle types and aggregation. Microbial degradation potentially played a more important role (Stephens et al. 2024), as small aggregates or detritus could be fragments of degraded fecal pellets. Functionally, these particle types may represent particles in a more advanced stage of microbial degradation compared to the other pellet categories. The particles that were categorized as aggregates were possibly highly degraded detritus with a loose structure. It also seems plausible that the aggregates and dense detritus in the deeper traps originated as fecal pellets at shallow depths. Moreover, physical processes including aggregation (Burd and Jackson 2009; Kiørboe 2001; Alldredge and Silver 1988) and disaggregation (Briggs et al. 2020; Song et al. 2023) which can result in morphological changes as particles sink over time, likely contributed to the uncertainty in the transfer efficiency of any particular particle class.

#### Discussion

GelCams provide an accessible tool for observing shorttime variations of particle fluxes occurring within the duration of a typical surface-tethered trap deployment. Their flexible, easily reproduced design should make them amenable to adaptation to a variety of trap platforms such as neutrally buoyant sediment traps or bottom-landing systems. These cameras, especially when used alongside other flux-measuring instruments, can be used to estimate carbon flux and variations among different particle types. The modeled POC fluxes from the GelCams generally agreed with ground truth measurements (Estapa et al. 2021; Durkin et al. 2021; Buesseler et al. 2020), although the current design does not resolve small particles such as the mini pellets described in other studies (Durkin et al. 2021). Although automated or deep learning methods were not implemented with this relatively small dataset, this is a feasible step that could enable onboard and

potentially real-time processing with future versions. In addition, sediment traps equipped with a GelCam offer several other ancillary advantages. By taking a continuous series of photographs of the trap contents, we can observe if and when swimmers arrive and any disruptions or changes that occur to the particles during the time spent in the trap before recovery. By tracking each individual particle over time, we can qualitatively observe if the particles are undergoing morphological changes or if the gel is effective in preserving their size and other characteristics.

Here we tried two different methods to model the timeresolved particle flux from the image sequences. The white pixel method and the tracking-based methods agreed with each other in terms of the cumulative particle areas. We recommend that an end user might make their own method selection based on processing time and desired data products. The white pixel method yielded a quick method to estimate the bulk particle flux but was affected by background ambient light variations between day and night. This method is similar to the attenuance-flux approach employed by Estapa et al. (2024) using optical sediment traps, except the attenuanceflux approach sums the attenuance values of each pixel, while the "white pixel method" here used the binarized images so each pixel had a value of unity (i.e., the method does not account for light intensities and transparency of particles). While more computationally intensive, the particle tracking method with classification was less affected by the day-night ambient light variation and provided information about the specific time of arrival of individual particles. These classifications allowed us to examine the relative importance of each particle type in the bulk flux. The GelCam framework thus generates a large data set that allows for both individual case studies and statistical analysis. Recovery and subsequent analysis of gel samples under an imaging microscope and through extraction for molecular or mineral analysis can reveal even more biological details and help with ground truthing (see Durkin et al. (2021)).

The GelCam prototype presented here also has a number of limitations that could (and will) be addressed with future technical improvements. A primary challenge was the variability in illumination. In this study, the red channel with a subsequent POD-based background removal was utilized to filter out variations in background lighting. The background lighting filtration was mostly effective, but some background patterns may still be visible during the daytime. Additionally, the RGB imaging system is based on a Bayer matrix, where red pixels constitute only 25% of the total and are potentially influenced by interpolated values from adjacent green and blue pixels (Gunturk et al. 2005). Extracting only the red channel results in the loss of 75% of the original pixel data, which reduces the effective spatial resolution. Future implementations would benefit from recording raw image data in the Bayer matrix format to mitigate these limitations.

Furthermore, the current pixel resolution was insufficient for detecting mini fecal pellets, as their size was smaller than one pixel. Particle classification also had uncertainty due to the manual identification, especially for small particles that just passed the detection threshold. Durkin et al. (2021) noted aggregates as one dominant population in the Subarctic North Pacific, but many aggregates were lost during the identification process because of their loose structures and transparent exopolymer particles (TEP) (Passow 2002; Azetsu-Scott and Passow 2004). Inevitably, we could not account for the contributions of organic carbon from TEP. We only resolved 2D images of particles from the single-camera imaging system. While we could predict the thickness of particles that retained regular shapes, such as long fecal pellets, particles prone to flattening within the gel would have more biased thickness predictions. These particles, such as especially delicate aggregates, tend to flatten and extend their projection areas when resting on a platform, thus leading to the overestimation of thickness based on assumptions of spherical shapes. In addition to uncalibrated 3D morphological information, 2D images resulted in the overlap of sub-images. For future improvements, capturing an additional view for 3D volume reconstruction, or establishing an empirical relationship for aggregate thickness, would be advantageous.

Hardware upgrades will enhance the GelCam design in the future. New GelCam iterations will configure the Pi camera with fixed parameters to ensure consistent and calibrated white balance, while saving the raw Bayer matrix format images with camera settings. Upgrading to more advanced camera modules with attached lenses will also generate a higher pixel resolution. Although it will still be challenging to detect small particles like mini fecal pellets ( $< 50 \mu m$ ), these improvements can reduce the detection limit of the imaging system. Additionally, the use of clear polycarbonate tubing, which introduces stray light interference, will be discontinued. While clear polycarbonate is commonly used due to its durability, lower cost, and transparency for removing seawater above the gel, future imaging trap tube designs will incorporate black tubing or apply specialized coatings to minimize light interference and variability (e.g., see SnoCam+; Edirisinghe et al. 2024). We are also exploring the integration of GelCam with Lagrangian floats. As Siegel and Deuser (1997) demonstrated, horizontal bulk flow is normally orders of magnitude greater than the sinking velocity, so replacing the surface tethered traps (STT) with neutrally buoyant sediment traps (NBST) could lead to an improved flux measurement. Furthermore, incorporating a swimmer exclusion device (e.g., the "labyrinth of doom"; Coale 1990) could be advisable. Although we could exclude swimmers during post-processing, the swimming zooplankton introduced additional uncertainty in the PIV analysis, and their vigorous activity, especially right after arrival in the gels, may disrupt and damage other particles (see Supporting Information videos).

The white pixel method can be further developed by building an empirical relation to the POC fluxes. This idea is not new. For example, Bishop et al. (2016) began with the projection area of particles, which was represented by binarized white pixels of individual particles in this study, and estimated carbon content from particle volume by empirically relating the thickness of particles to their equivalent circular diameter. Later, using calibration samples with OSR, Bourne et al. (2021) calculated volume attenuance flux from particle subimages and empirically converted it into POC flux. Similarly, Estapa et al. (2024) correlated total light attenuance of particles with the POC flux. We did not apply any of these empirical relations because particles were illuminated from the side (not behind as required for an attenuance estimate), particle areas were corrected based on lighting, and particles preserved in the gel layer did not become fully flattened due to gravity. Building a reliable relation requires extensive datasets collected by GelCam and other similar instruments featuring upward-facing cameras and side lighting (i.e., quasi-darkfield illumination). Lastly, implementing an automated particle classification process will be beneficial to reduce the labor of processing subimages manually. Leveraging machine learning methods will provide significant insights into the model of carbon export (Irisson et al. 2022; Trudnowska et al. 2021; Amaral and Durkin 2025).

#### **Author Contributions**

Yixuan Song: Methodology (equal); formal analysis (lead); data curation; writing—original draft (lead); review and editing (equal). Melissa Omand: Conceptualization (lead); methodology (equal); data collection (equal); funding acquisition (equal); writing—original draft (supporting); writing—review and editing (equal). Colleen A. Durkin: Conceptualization (supporting); data collection (equal); funding acquisition (equal); writing—review and editing (equal). Margaret L. Estapa: Conceptualization (supporting); data collection (equal); writing—review and editing (equal). Ken O. Buesseler: Conceptualization (supporting); data collection (equal); funding acquisition (equal); writing—review and editing (equal).

#### **Acknowledgments**

We wish to thank Nils Haentjens, Vinicius Amaral, Roger Patrick Kelly, Sean O'Neil, Alyson Santoro, Nicola Paul, and the EXPORTS team for assistance with data collection, their helpful discussions, and constructive recommendations. We are also grateful to the captains and crew of the R/V Revelle and R/V James Cook. We would like to thank the anonymous reviewers for their detailed and insightful comments, particularly on the discussion of Bayer matrix effects, which significantly improved the manuscript. Data collected through this project was supported by NASA Grants 80NSSC17K0662 and

80NSSC21K0015. Postdoctoral support for Yixuan Song was provided by the Oceankind foundation.

#### **Conflicts of Interest**

None declared.

#### **Data Availability Statement**

The data that support the findings of this study are openly available in NASA's SeaBASS archive at https://oceandata.sci.gsfc.nasa.gov/ob/getfile/dd2fe323be\_EXPORTS-EXPORTSNP\_RR1813\_GelCam\_20180814-20180909\_R1.sb and https://oceandata.sci.gsfc.nasa.gov/ob/getfile/8a0152ccab\_EXPORTS-EXPORTSNA\_JC214\_GelCam\_20210504-20210509\_R1.sb. The MATLAB code we developed for particle tracking is available at https://github.com/EE-Shuan-Song/GelCam\_particle\_tracking.

#### References

Alldredge, A. L., and C. Gotschalk. 1988. "In Situ Settling Behavior of Marine Snow." *Limnology and Oceanography* 33, no. 3: 339–351. https://doi.org/10.4319/lo.1988.33.3.0339.

Alldredge, A. L., and M. W. Silver. 1988. "Characteristics, Dynamics and Significance of Marine Snow." *Progress in Oceanography* 20, no. 1: 41–82. https://doi.org/10.1016/0079-6611(88)90053-5.

Amaral, V. J., and C. A. Durkin. 2025. "A Computer Vision-Based Approach for Estimating Carbon Fluxes From Sinking Particles in the Ocean." *Limnology and Oceanography: Methods* 23, no. 2: 117–130. https://doi.org/10.1002/lom3. 10665.

Asper, V. L. 1987. "Measuring the Flux and Sinking Speed of Marine Snow Aggregates." *Deep Sea Research Part A. Oceanographic Research Papers* 34, no. 1: 1–17. https://doi.org/10.1016/0198-0149(87)90117-8.

Azetsu-Scott, K., and U. Passow. 2004. "Ascending Marine Particles: Significance of Transparent Exopolymer Particles (TEP) in the Upper Ocean." *Limnology and Oceanography* 49, no. 3: 741–748. https://doi.org/10.4319/lo.2004.49.3.0741.

Billett, D. S. M., R. S. Lampitt, A. L. Rice, and R. F. C. Mantoura. 1983. "Seasonal Sedimentation of Phytoplankton to the Deep-Sea Benthos." *Nature* 302, no. 5908: 520–522. https://doi.org/10.1038/302520a0.

Bishop, J. K. B., M. B. Fong, and T. J. Wood. 2016. "Robotic Observations of High Wintertime Carbon Export in California Coastal Waters." *Biogeosciences* 13, no. 10: 3109–3129. https://doi.org/10.5194/bg-13-3109-2016.

Bisson, K., D. A. Siegel, and T. DeVries. 2020. "Diagnosing Mechanisms of Ocean Carbon Export in a Satellite-Based Food Web Model." *Frontiers in Marine Science* 7: 505. https://doi.org/10.3389/fmars.2020.00505.

Bourne, H. L., J. K. B. Bishop, E. J. Connors, and T. J. Wood. 2021. "Carbon Export and Fate Beneath a Dynamic Upwelled Filament Off the California Coast." *Biogeosciences* 

- 18, no. 10: 3053–3086. https://doi.org/10.5194/bg-18-3053-2021.
- Briggs, N., G. Dall'Olmo, and H. Claustre. 2020. "Major Role of Particle Fragmentation in Regulating Biological Sequestration of CO<sub>2</sub> by the Oceans." *Science* 367, no. 6479: 791–793. https://doi.org/10.1126/science.aay1790.
- Bruland, K. W., and M. W. Silver. 1981. "Sinking Rates of Fecal Pellets From Gelatinous Zooplankton (Salps, Pteropods, Doliolids)." *Marine Biology* 63, no. 3: 295–300. https://doi.org/10.1007/BF00395999.
- Buesseler, K. O., A. N. Antia, M. Chen, et al. 2007. "An Assessment of the Use of Sediment Traps for Estimating Upper Ocean Particle Fluxes." *Journal of Marine Research* 65, no. 3: 345–416. https://doi.org/10.1357/002224007781567621.
- Buesseler, K. O., C. R. Benitez-Nelson, M. Roca-Mart'ı, et al. 2020. "High-Resolution Spatial and Temporal Measurements of Particulate Organic Carbon Flux Using Thorium-234 in the Northeast Pacific Ocean During the Export Processes in the Ocean from Remote Sensing Field Campaign." *Elementa: Science of the Anthropocene* 8, no. 1: 030. https://doi.org/10.1525/elementa.2020.030.
- Burd, A. B., and G. A. Jackson. 2009. "Particle Aggregation." *Annual Review of Marine Science* 1, no. 1: 65–90. https://doi.org/10.1146/annurev.marine.010908.163904.
- Cavan, E. L., S. A. Henson, A. Belcher, and R. Sanders. 2017. "Role of Zooplankton in Determining the Efficiency of the Biological Carbon Pump." *Biogeosciences* 14, no. 1: 177–186. https://doi.org/10.5194/bg-14-177-2017.
- Coale, K. H. 1990. "Labyrinth of Doom: A Device to Minimize the "Swimmer" Component in Sediment Trap Collections." *Limnology and Oceanography* 35, no. 6: 1376–1381. https://doi.org/10.4319/lo.1990.35.6.1376.
- Collins, J. R., B. R. Edwards, K. Thamatrakoln, et al. 2015. "The Multiple Fates of Sinking Particles in the North Atlantic Ocean." *Global Biogeochemical Cycles* 29, no. 9: 1471–1494. https://doi.org/10.1002/2014GB0 05037.
- Dall'Olmo, G., J. Dingle, L. Polimene, R. J. W. Brewin, and H. Claustre. 2016. "Substantial Energy Input to the Mesopelagic Ecosystem From the Seasonal Mixed-Layer Pump." *Nature Geoscience* 9, no. 11: 820–823. https://doi.org/10.1038/ngeo2818.
- DeVries, T., and T. Weber. 2017. "The Export and Fate of Organic Matter in the Ocean: New Constraints From Combining Satellite and Oceanographic Tracer Observations." *Global Biogeochemical Cycles* 31, no. 3: 535–555. https://doi.org/10.1002/2016GB005551.
- Durkin, C. A., K. O. Buesseler, I. Cetini'c, M. L. Estapa, R. P. Kelly, and M. Omand. 2021. "A Visual Tour of Carbon Export by Sinking Particles." *Global Biogeochemical Cycles* 35, no. 10: e2021GB006985. https://doi.org/10.1029/2021GB006985.
- Edirisinghe, S., Y. Song, P. Roberts, et al. 2024. "SnoCam+: An Open-Source, Trap-Deployable Imaging System for Sinking

- Particles in the Ocean." In 2024 Ocean Sciences Meeting. American Geophysical Union.
- Estapa, M., K. Buesseler, C. A. Durkin, et al. 2021. "Biogenic Sinking Particle Fluxes and Sediment Trap Collection Efficiency at Ocean Station Papa." *Elementa: Science of the Anthropocene* 9, no. 1: 00122. https://doi.org/10.1525/elementa.2020.00122.
- Estapa, M. L., C. A. Durkin, W. H. Slade, C. L. Huffard, S. P. O'Neill, and M. M. Omand. 2024. "A New, Global Optical Sediment Trap Calibration." *Limnology and Oceanography: Methods* 22, no. 2: 77–92. https://doi.org/10.1002/lom3.10592.
- Friedlingstein, P., M. O'Sullivan, M. W. Jones, et al. 2023. "Global Carbon Budget 2023." *Earth System Science Data* 15, no. 12: 5301–5369. https://doi.org/10.5194/essd-15-5301-2023.
- Gowing, M. M., and M. W. Silver. 1985. "Minipellets: A New and Abundant Size Class of Marine Fecal Pellets." *Journal of Marine Research* 43, no. 2: 395–418. https://doi.org/10.1357/002224085788438676.
- Gunturk, B. K., J. Glotzbach, Y. Altunbasak, R. W. Schafer, and R. M. Mersereau. 2005. "Demosaicking: Color Filter Array Interpolation." *IEEE Signal Processing Magazine* 22, no. 1: 44–54. https://doi.org/10.1109/MSP.2005.1407714.
- Henson, S. A., C. Laufkotter, S. Leung, S. L. C. Giering, H. I. Palevsky, and E. L. Cavan. 2022. "Uncertain Response of Ocean Biological Carbon Export in a Changing World." *Nature Geoscience* 15, no. 4: 248–254. https://doi.org/10.1038/s41561-022-00927-0.
- Henson, S. A., R. Sanders, E. Madsen, P. J. Morris, F. Le Moigne, and G. D. Quartly. 2011. "A Reduced Estimate of the Strength of the Ocean's Biological Carbon Pump." *Geophysical Research Letters* 38, no. 4: L04606. https://doi.org/ 10.1029/2011GL046735.
- Huffard, C. L., C. A. Durkin, S. E. Wilson, P. R. McGill, R. Henthorn, and K. L. Smith. 2020. "Temporally-Resolved Mechanisms of Deep-Ocean Particle Flux and Impact on the Seafloor Carbon Cycle in the Northeast Pacific." *Deep Sea Research Part II: Topical Studies in Oceanography* 173: 104763. https://doi.org/10.1016/j.dsr2.2020.104763.
- Irisson, J.-O., S.-D. Ayata, D. J. Lindsay, L. Karp-Boss, and L. Stemmann. 2022. "Machine Learning for the Study of Plankton and Marine Snow From Images." *Annual Review of Marine Science* 14, no. 1: 277–301. https://doi.org/10.1146/annurev-marine-041921-013023.
- Kiørboe, T. 2001. "Formation and Fate of Marine Snow: Small-Scale Processes With Large-Scale Implications." *Scientia Marina* 65, no. S2: 57–71. https://doi.org/10.3989/scimar. 2001.65s257.
- McDonnell, A. M. P., and K. O. Buesseler. 2010. "Variability in the Average Sinking Velocity of Marine Particles." *Limnology and Oceanography* 55, no. 5: 2085–2096. https://doi.org/10.4319/lo.2010.55.5.2085.
- McGill, P. R., R. G. Henthorn, L. E. Bird, C. L. Huffard, D. V. Klimov, and K. L. Smith. 2016. "Sedimentation Event

- Sensor: New Ocean Instrument for In Situ Imaging and Fluorometry of Sinking Particulate Matter." *Limnology and Oceanography: Methods* 14: 853–863. https://doi.org/10.1002/lom3.10131.
- Mendez, M., M. Raiola, A. Masullo, et al. 2017. "POD-Based Background Removal for Particle Image Velocimetry." *Experimental Thermal and Fluid Science* 80: 181–192. https://doi.org/10.1016/j.expthermflusci.2016.08.021.
- Müller, P., and E. Suess. 1979. "Productivity, Sedimentation Rate, and Sedimentary Organic Matter in the Oceans—I. Organic Carbon Preservation." *Deep-Sea Research Part A, Oceanographic Research Papers* 26, no. 12: 1347–1362. https://doi.org/10.1016/0198-0149(79)90003-7.
- Nobach, H., and M. Honkanen. 2005. "Two-Dimensional Gaussian Regression for Sub-Pixel Displacement Estimation in Particle Image Velocimetry or Particle Position Estimation in Particle Tracking Velocimetry." *Experiments in Fluids* 38, no. 4: 511–515. https://doi.org/10.1007/s00348-005-0942-3.
- Nowicki, M., T. DeVries, and D. A. Siegel. 2022. "Quantifying the Carbon Export and Sequestration Pathways of the Ocean's Biological Carbon Pump." *Global Biogeochemical Cycles* 36, no. 3: e2021GB007083. https://doi.org/10.1029/2021GB007083.
- Omand, M. M., E. A. D'Asaro, C. M. Lee, et al. 2015. "Eddy-Driven Subduction Exports Particulate Organic Carbon From the Spring Bloom." *Science* 348, no. 6231: 222–225. https://doi.org/10.1126/science.1260062.
- Otsu, N. 1979. "A Threshold Selection Method From Gray-Level Histograms." *IEEE Transactions on Systems, Man, and Cybernetics* 9, no. 1: 62–66. https://doi.org/10.1109/TSMC. 1979.4310076.
- Passow, U. 2002. "Transparent Exopolymer Particles (TEP) in Aquatic Environments." *Progress in Oceanography* 55, no. 3–4: 287–333. https://doi.org/10.1016/S0079-6611(02) 00138-6.
- Piao, S., S. Sitch, P. Ciais, et al. 2013. "Evaluation of Terrestrial Carbon Cycle Models for Their Response to Climate Variability and to CO<sub>2</sub> Trends." *Global Change Biology* 19, no. 7: 2117–2132. https://doi.org/10.1111/gcb.12187.
- Siegel, D. A., I. Cetini'c, J. R. Graff, et al. 2021. "An Operational Overview of the Export Processes in the Ocean from Remote Sensing (EXPORTS) Northeast Pacific Field Deployment." *Elementa: Science of the Anthropocene* 9, no. 1: 00107. https://doi.org/10.1525/elementa.2020.00107.
- Siegel, D., and W. Deuser. 1997. "Trajectories of Sinking Particles in the Sargasso Sea: Modeling of Statistical Funnels Above Deep-Ocean Sediment Traps." *Deep Sea Research, Part I: Oceanographic Research Papers* 44, no. 9–10: 1519–1541. https://doi.org/10.1016/S0967-0637(97)00028-9.
- SierraI, C. A., M. E. Harmon, F. H. Moreno, S. A. Orrego, and J. I. Del Valle. 2007. "Spatial and Temporal Variability of Net

- Ecosystem Production in a Tropical Forest: Testing the Hypothesis of a Significant Carbon Sink." *Global Change Biology* 13, no. 4: 838–853. https://doi.org/10.1111/j.1365-2486. 2007.01336.x.
- Song, Y., A. B. Burd, and M. J. Rau. 2023. "The Deformation of Marine Snow Enables its Disaggregation in Simulated Oceanic Shear." *Frontiers in Marine Science* 10: 1224518. https://doi.org/10.3389/fmars.2023.1224518.
- Song, Y., and M. J. Rau. 2022. "A Novel Method to Study the Fragmentation Behavior of Marine Snow Aggregates in Controlled Shear Flow." *Limnology and Oceanography: Methods* 20, no. 10: 618–632. https://doi.org/10.1002/lom3. 10509.
- Steinberg, D. K., K. Stamieszkin, A. E. Maas, et al. 2023. "The Outsized Role of Salps in Carbon Export in the Subarctic Northeast Pacific Ocean." *Global Biogeochemical Cycles* 37, no. 1: e2022GB007523. https://doi.org/10.1029/2022GB007523.
- Stephens, B. M., C. A. Durkin, G. Sharpe, et al. 2024. "Direct Observations of Microbial Community Succession on Sinking Marine Particles." *ISME Journal* 18, no. 1: wrad010. https://doi.org/10.1093/ismejo/wrad010.
- Thielicke, W., and E. J. Stamhuis. 2014. "PIVlab—Towards User-Friendly, Affordable and Accurate Digital Particle Image Velocimetry in MATLAB." *Journal of Open Research Software* 2: e30. https://doi.org/10.5334/jors.bl.
- Trudnowska, E., L. Lacour, M. Ardyna, et al. 2021. "Marine Snow Morphology Illuminates the Evolution of Phytoplankton Blooms and Determines Their Subsequent Vertical Export." *Nature Communications* 12, no. 1: 2816. https://doi.org/10.1038/s41467-021-22994-4.
- Westerweel, J., and F. Scarano. 2005. "Universal Outlier Detection for PIV Data." *Experiments in Fluids* 39: 1096–1100. https://doi.org/10.1007/s00348-005-0016-6.
- Wilson, J. D., O. Andrews, A. Katavouta, et al. 2022. "The Biological Carbon Pump in CMIP6 Models: 21st Century Trends and Uncertainties." *Proceedings of the National Academy of Sciences of the United States of America* 119, no. 29: e2204369119. https://doi.org/10.1073/pnas.2204369119.

#### **Supporting Information**

Additional Supporting Information may be found in the online version of this article.

Submitted 15 April 2025 Revised 28 July 2025 Accepted 04 August 2025